Multiple direction needle-path planning and inverse dose optimization for robotic low-dose rate brachytherapy

Philipp Aumüller[1,*], **Andreas Rothfuss**[2], **Martin Polednik**[1], **Yasser Abo-Madyan**[1], **Michael Ehmann**[1], **Frank A. Giordano**[3], **Sven Clausen**[1]

[1] Department of Radiation Oncology, University Medical Centre Mannheim, University Heidelberg, Germany
[2] Fraunhofer IPA, Mannheim, Germany
[3] Department of Radiation Oncology, University Hospital Bonn, University of Bonn, Germany

Received 11 February 2021; accepted 7 June 2021

Abstract

Purpose: *Robotic systems to assist needle placements for low-dose rate brachytherapy enable conformal dose planning only restricted to path planning around risk structures. We report a treatment planning system (TPS) combining multiple direction needle-path planning with inverse dose optimization algorithms.*

Methods: *We investigated in a path planning algorithm to efficiently locate needle injection points reaching the target volume without puncturing risk structures. A candidate needle domain with all combinations of trajectories is used for the optimization process. We report a modular algorithm for inverse radiation plan optimization. The initial plan with $V100 > 99\%$ is generated by the "greedy optimizer". The "remove-seed algorithm" reduces the number of seeds in the high dose regions. The "depth-optimizer" varies the insertion depth of the needles. The "coverage-optimizer" locates under-dosed areas in the target volume and supports them with an additional amount of seeds. The dose calculation algorithm is benchmarked on an image set of a phantom with a liver metastasis (prescription dose $D_{pr} = 100\,Gy$) and is re-planned in a commercial CE-marked TPS to compare the calculated dose grids using a global gamma analysis. The inverse optimizer is benchmarked by calculating 10 plans on the same phantom to investigate the stability and statistical variability of the dose parameters.*

Results: *The path planning algorithm efficiently removes 72.5% of all considered injection points. The candidate needle domain consists of combinations of 1971 tip points and 827 injection points. The global gamma analysis with gamma $1\% = 2.9\,Gy$, $1\,mm$ showed a pass rate of 98.5%. The dose parameters were $V100 = (99.1 \pm 0.3)\,\%$, $V150 = (76.4 \pm 2.5)\,\%$, $V200 = (44.5 \pm 5.5)\,\%$ and $D90 = 125.9 \pm 3.6\,Gy$ and 10.7 ± 1.3 needles with 34.0 ± 0.8 seeds were used. The median of the TPS total running time was 4.4 minutes.*

Conclusions: *The TPS generates treatment plans with acceptable dose coverage in a reasonable amount of time. The gamma analysis shows good accordance to the commercial TPS. The TPS allows taking full advantage of robotic navigation tools to enable a new precise and safe method of minimally invasive low-dose-rate brachytherapy.*

Keywords: Brachytherapy, LDR, Seeds, Robotic, Path planning, Inverse optimization

* Corresponding author: Philipp Aumüller, Department of Radiation Oncology, University Medical Centre Mannheim, University Heidelberg, Germany.
E-mail: philipp.aumueller@medma.uni-heidelberg.de (P. Aumüller).

Z Med Phys **32** (2022) 173–187
https://doi.org/10.1016/j.zemedi.2021.06.003
www.elsevier.com/locate/zemedi
© 2021 The Author(s). Published by Elsevier GmbH on behalf of DGMP, ÖGMP and SSRMP. This is an open access article under the CC BY-NC-ND license (http://creativecommons.org/licenses/by-nc-nd/4.0/).

1 Introduction

Low-dose-rate (LDR) brachytherapy is an established method for the treatment of early staged prostate carcinoma [1] with excellent local tumour control [2] while preserving a high quality of life [3]. The method relies on placement of radioactive emitters (seeds) in the prostate through a mounted grid under guidance with trans-rectal ultrasound (TRUS) [4]. However the routinely used imaging method based on trans-rectal ultrasound is restricted to prostate brachytherapy.

The first approach to treat other tumour sites was intraoperative seed implantation, where the target volume could be defined under sight within the tumour bed. From the 80s to the early 2000s, unresectable liver metastases [5], pancreatic cancers [6,7], tumours causing spinal cord compression [8] and lung cancer [9] were treated with intraoperative treatment. With upcoming computer tomography (CT) free-hand percutaneous seed implantation was shown for these tumour regions as well [10,11] enabling a minimal invasive therapy. However, this method requires a high skill of the physician to precisely implant the needle to the desired position. More recent research aims to use 3D printing for individualised implantation templates for coplanar [12] and non-coplanar needles [13] in combination with hybrid optimization of the treatment plan by placing needles virtually. A simulated annealing optimizer is then used to find the optimal number of seeds [14].

Novel technical innovations are robotic assistants as navigation tools. A study comparing the latter with free hand intervention shows an improved needle placement accuracy [15]. We recently described an approach using a robotic arm that is able to move precisely to the desired location on the patient's skin [16]. The fixed template as current state of the art was replaced by an injection device connected to the robot while the needle injection remains task of the physician. The robot can be classified as a Level II robot after the AAPM 192 guidelines [17]. We expect to reduce the geometric position error of the seeds with an improved implantation precision. The latter is of major importance to the post-implantation dose distribution due to the steep dose gradient of the seeds low keV photon emission.

This technical improvement enables to inject needles from multiple directions giving a high flexibility to the degrees of freedom to reach difficult target volumes surrounded by complex risk structures. The robotic automatisation can lead to a standardized workflow for various tumour sites while optimizing it in terms of safeness, precision and time efficiency.

To make use of these possibilities we need an inverse planning system containing the needle-path planning and an inverse dose optimization. Siauw et al. [18] introduced the method to generate a candidate needle domain for skew catheters in a defined plane in the prostate for high-dose rate brachytherapy. In our work we were inspired by this approach to calculate a candidate needle domain containing all possible needle trajectories based on path planning avoiding critical structures and bones. The second part is to use this needle candidate domain for the inverse treatment planning. Here we report a 4-step algorithm. A novel greedy optimizer covers the target volume with the prescription dose. The other 3 steps optimize the initial plan by removing seeds, variating the insertion depth and setting additional needles to cover the target volume.

2 Materials and Methods

2.1 The workflow and setup of the system

We used a complex, novel abdominal phantom containing a liver metastasis (40.3 ml) as a treatment example (Figure 1 and Figure 2).

The workflow (Figure 1) starts with a cone-beam CT (CBCT) of the abdomen, generated with Artis Zeego (Siemens, Erlangen), a robotic angiography system. The target volume as well as risk structures and bones are contoured on the image set with a commercial treatment planning system (Oncentra Prostate, Nucletron-v4.0). The structure information is imported as RT-struct files with the scripts of [19] in the here presented new TPS based on MATLAB (The MathWorks-R2020a). The contour points are used to generate 3D volumes with the MATLAB alphaShape function based on Delaunay triangulation [20,21]. The initialised volumes are shown in Figure 2 containing the metastasis as the target volume, the liver, aorta, vena cava and the ribs as risk structures. The path planner (section 2.2) locates the injection coordinates for the needle trajectories. The candidate needle domain contains all combinations of needle injection- and tip coordinates (section 2.3). Then the inverse optimization steps (sections 2.5–2.8) generate a treatment plan within the given dose constraints. The robotic assistant receives the first needle trajectory and places the injection template automatically to the planned injection point. The physician injects the needle and verifies the position with fluoroscopy. This paper focuses on the TPS with an imported structure set as a starting point and the accepted treatment plan as the end point. The test case target volume is a liver metastasis which we assume to treat with $D_{pr} = 100\,\mathrm{Gy}$ prescribed to the covering isodose. For metastases with no organ at risk in close distance (like the aorta and vena cava in the test case) higher prescription doses are possible. In the study of Martinez-Monge et al. [5] e.g. the peripheral dose of liver metastases was prescribed to 144 Gy. For the dose evaluation we used the $V100$, $V150$, $V200$ indicating the percentage of the target volume receiving at least $(100, 150, 200)\,\%$ of the prescription dose D_{pr}. We aim to achieve a high V100 (percentage of the target volume receiving 100% of D_{pr}) value in the range of (97–100)% a $V200$ value as low as achievable as well as a $D90 > 120\%$. The $D90$ indicates the minimum dose of 90% of the target volume and can be related directly to clinical outcome for other treatments such as prostate seed brachytherapy [22]. For the path

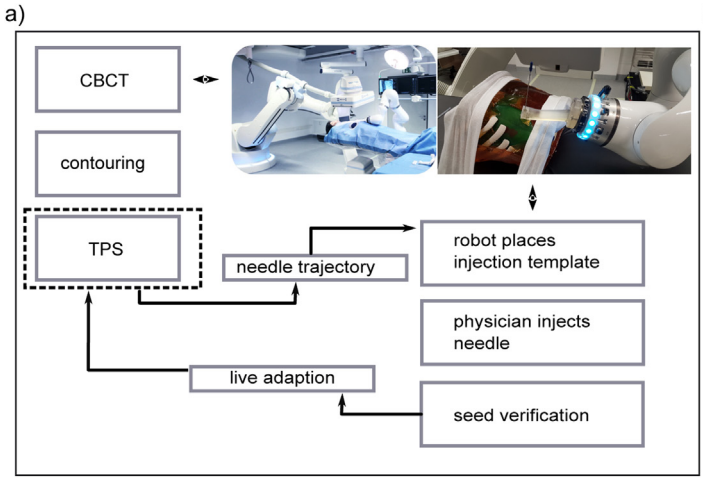

Figure 1. a) The workflow and experimental setup. Left picture: The robotic angiography system. Right picture: The abdomen phantom and the robotic assistant with the injection template. b) The work steps of the treatment planning system.

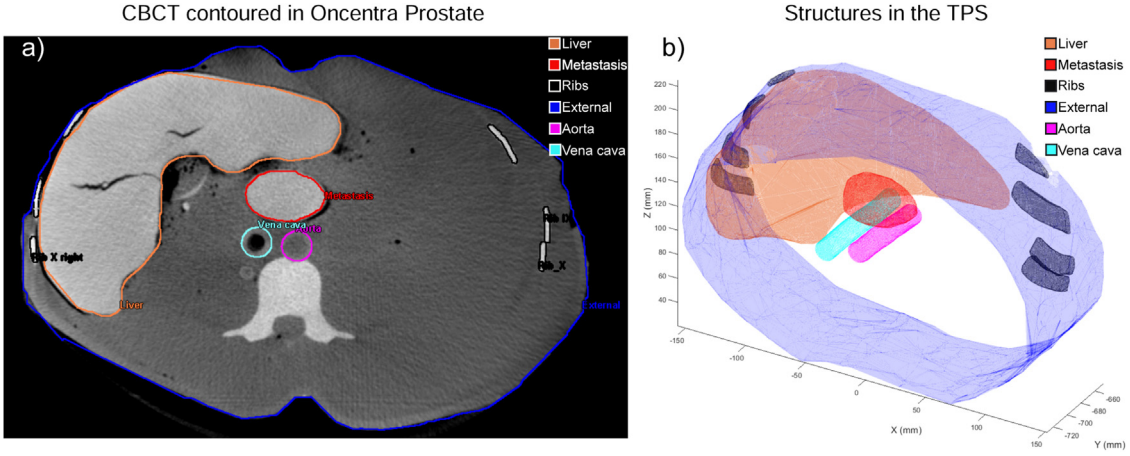

Figure 2. a) The contoured CBCT of the phantom in Oncentra Prostate. b) The imported structures in the TPS.

planning there are the liver and the ribs to be considered as forbidden structures for needle insertion.

We used a Windows 10 computer with an Intel® Core™ i5-6500 CPU with 3.2 Ghz, 16.0 GB RAM and a NVIDIA NVS 510 graphics card.

2.2 The path planner

The path planner identifies the domain of injection coordinates on the patient's surface suitable to puncture the target volume and to avoid risk structures. The coordinate points defining the patient's external contour are considered as possible injection points and are filtered with the following algorithms. As the patient is lying on his back on a treatment couch the injection points with a sagittal component (z-component) smaller than the z-component of the median of the patient's surface contour are filtered out.

To filter trajectories through organs at risk and bones a new algorithm has been developed. It uses the MATLAB function *inShape* to determine if a specific point lies in or outside of a given alpha shape [23]. If a specified checkpoint of a trajectory is located inside of a risk structure, the referring injection point is filtered out. In the first step the checkpoint is calculated as follows.

The trajectory of the needle can be defined by the injection point IP_i and the tip point TP of the needle with i indexing the position in the array of injection points. The tip point TP of all trajectories is set to the median of the target volume.

The unit vector of the needle trajectory from tip to injection is $\frac{\vec{\lambda}_i}{|\vec{\lambda}_i|}$, with $\vec{\lambda}_i = \vec{IP}_i - \vec{TP}$. The checkpoints ($CP_i$) are located on these trajectories and calculated with

$$\vec{CP}_i = \vec{TP} + r * \frac{\vec{\lambda}_i}{|\vec{\lambda}_i|}, \tag{1}$$

r being the distance of the median of the risk structure M_R to the median of the target volume. Then the checkpoints are located on a surface of a sphere with the radius r. The index i now connects the checkpoint CP_i to the injection point IP_i that is lying on its trajectory to $\vec{TP}$. All IP_i with CP_i inside of the risk structure are filtered out.

Now more specific filters are used to find remaining invalid injection points. The median of the risk structure M_R is varied by

$$M_R^{'}(x, y, z) = M_R(x, y, z) + (\delta * std(M_R(x, y, z))), \quad (2)$$

with $\delta = [-2 : 0.1 : 2]$ and $std\,(M_R\,(x, y, z))$ being the standard deviation of the risk structures contour points to the median. The raster of $\delta * std\,(M_R\,(x, y, z))$ scans the range of 2 standard deviations which includes about 95% of normally distributed data taking a possible geometric asymmetry of the risk structures around their median into account.

The tip point TP is varied by setting it on the target volumes contour surface. The latter 6 tip points are the contours maxima and minima of each room direction x, y, z. The length of the 18 Gauge Needles is in total 22.5 cm with 20 cm insertion depth and the path length inside of the patient is constraint to 17.5 cm calculated for trajectories to the most posterior contour point in the −z direction. To further decrease the number of injection points and to speed up the optimization process injection points with a distance below 2 mm to the next injection point are filtered out.

The remaining injection points are used to calculate a domain of needle candidates used for the treatment plan optimization. During the optimization process (sections 2.5 and 2.8) each chosen needle trajectory is divided into points of 1 cm distance to be checked for collisions with risk structures.

2.3 Needle candidate domain

The contour points cp of the target volume TV fulfilling the condition

$$cp\,(z) < median\,(TV\,(z)) + 1.5 * std\,(TV\,(z)) \quad (3)$$

are considered as possible tip points TP_j for the needle candidates, with j indexing the array of needle tips. The tip points with a distance below 1 mm are filtered out to speed up the optimisation. Table 1 shows the structure of the needle candidate domain.

For every needle tip there is a domain of injection coordinates associated depending on the number of stranded seeds per needle. It is defined that the seeds have to be placed inside the target volume. The position of the nth seed s_n of the $(j,i)^{th}$ needle is

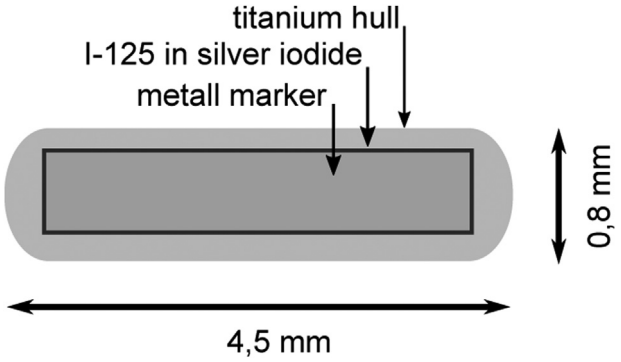

Figure 3. The structure and size of an Iodine-125 seed.

$$s_n = TP_j + \left[((n-1) * L_{cc}) + L_{tip} + \frac{L_{seed}}{2}\right] * \frac{\vec{\lambda_i}}{|\vec{\lambda_i}|}, \quad (4)$$

with L_{cc} and L_{seed} the length of the seed and distance from the seeds' centre to centre as displayed in Figure 3 and Figure 4 and L_{tip} the length of the needle tip. The inShape function is used to filter the domain of injection points for each tip point and seed number. The maximum number of seeds per needle is set to $n_{max} = 5$. This domain is used for the inverse planning process by navigating through the domain with loops over j, i.

2.4 Seed and dose modelling

Seed strands are used to implant several seeds per needle to improve the implant accuracy and to avoid single seed displacement and rotation [24]. The size and structure of the seeds are shown in Figure 3. The photon emission of the implanted Iodine-125 seeds with the weighted mean photon energy of $E_\gamma = 28.37$ keV [25] results in a steep dose gradient that allows a high dose in the target volume and a minimized dose in surrounding tissues [4].

The seeds radiation dose is modelled with the TG-43 line source (2D) formalism [25] with the seed source BEGIG model S17plus 125-I [26] used in our department. The air kerma strength per seed is set to $0.838U$.

In TG-43 the dose rate of a seed depends on the distance r and the polar angle Θ between the calculation point and the seed centre. The dose rates are given up to a distance $r = 2.5$ mm in [26] used as a basis for the dose calculation. To have an estimation of the steep dose gradient of the seed, the dose rate is extrapolated to the distances $r = \{1, 2\}$ mm

Table 1
The structure of the candidate needle domain represented as a cell array in the TPS. Each of the first column cells contains the coordinates of a needle tip. The other column cells contain the domain of all injection coordinates in reference to the needle tip of the same row with the column number specifying the number of seeds of each needle.

Needle tip coordinate (x, y, z)	Domain of injection coordinates (x, y, z) for a needle with a n seed strand				
	n = 1	n = 2	n = 3	n = 4	n = 5
1st needle tip (x, y, z)	{injection coordinates (x, y, z)}	...			
...					

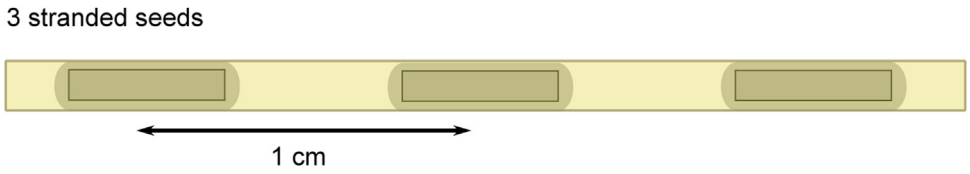

Figure 4. A 3 seed strand with spacers of 5.5 mm length. The distance from the seeds' centre to centre is 1 cm.

as well as to the seeds surface. The distance from the seeds centre to the seeds surface r_{surf} can be calculated with

$$r_{surf}(\Theta) = \frac{\frac{d_{\text{seed}}}{2}}{\sin(\Theta)}. \tag{5}$$

For each angle Θ_i the dose rate values $\dot{D}_{\Theta_i}(r)$ are fitted with the power function $f(x) = a * x^b$. Then the surface dose rate is

$$\dot{D}_{\Theta_i}(r_{surf}) = a * r_{surf}^b, \tag{6}$$

with a and b resulting from the fit. These fit functions are also used to interpolate the dose rate to the distances $r = \{3, 4, 6, 7\}$ mm. The dose rate modelling ranges from the seed surface up to 10 cm radial distance.

The dose rates are numerically integrated over the time to calculate the dose grid.

The resulting 2D polar dose distribution $D(r, \Theta)$ is vectorised to calculate a spherical 3D dose grid $D(r, \Theta, \phi)$ using the rotational symmetry of the cylindrical seed. It is used to interpolate to a Cartesian 3D dose grid $D(x, y, z)$. The inter- and extrapolation of the dose rate minimizes the error of linear interpolation by the huge amount of grid points in the seed's near field $r = \{r_{surf}, 7\,\text{mm}\}$.

To calculate the seed dose with a specific location and alignment the grid is translated and rotated accordingly. Each grid is interpolated and summed on a central dose grid in the target space to calculate the dose of the total implant. The dose distribution of a 5 seed strand is displayed in Figure 5.

To validate the $(1 * 1 * 1)\,\text{mm}^3$ dose grid of a treatment plan the needles are re-planned in the commercial planning system Oncentra Prostate (Nucletron-v4.0) by placing them according to the DICOM coordinates of the image set. 2 representative dose planes are compared with a global gamma analysis in the commercial software OmniPro I'mRT (IBA-1.7b).

2.5 Greedy optimizer

The inverse greedy optimizer is used to calculate an initial treatment plan with high prescription dose coverage of the target volume $V100 > 99\%$. The result is the initial plan configuration, an array containing the needles' tip- and injection points and the number of seeds. Needles are added sequentially and irreversible to the target space contributing to the dose distribution. With this the optimization problem is divided in sub-problems that are solved by maximizing the objective function. This procedure is well known as a greedy heuristic used for prostate brachytherapy optimisation as well [27]. The resulting plan configuration can be seen as a local optimum of the optimization problem.

Due to the huge amount of possible needle combinations there may be a comparably large number of valid needle combinations matching our treatment aims. To benchmark the stability and statistical variability of this optimizer 10 plans for the given problem are calculated.

The starting point is the first needle chosen by the following statistical considerations. The needle tip is the one associated with the highest number of injection points for needles with the maximum number of seeds $n_{max} = 5$. The geometrical median of the domain of injection points is the injection point used to define the first needle with 5 seeds. The following algorithm is executed in a loop that stops when the threshold $V100 > 99\%$ is passed. The dose of the actual needle configuration is calculated. The candidate needle domain is filtered to decrease the number of considered needles and the number of objective function calls. The needle tips have to be located in the dose range of

$$DR = \left[0.25 * D_{pr}, 0.7 * D_{pr} + 3 * N\right], \tag{7}$$

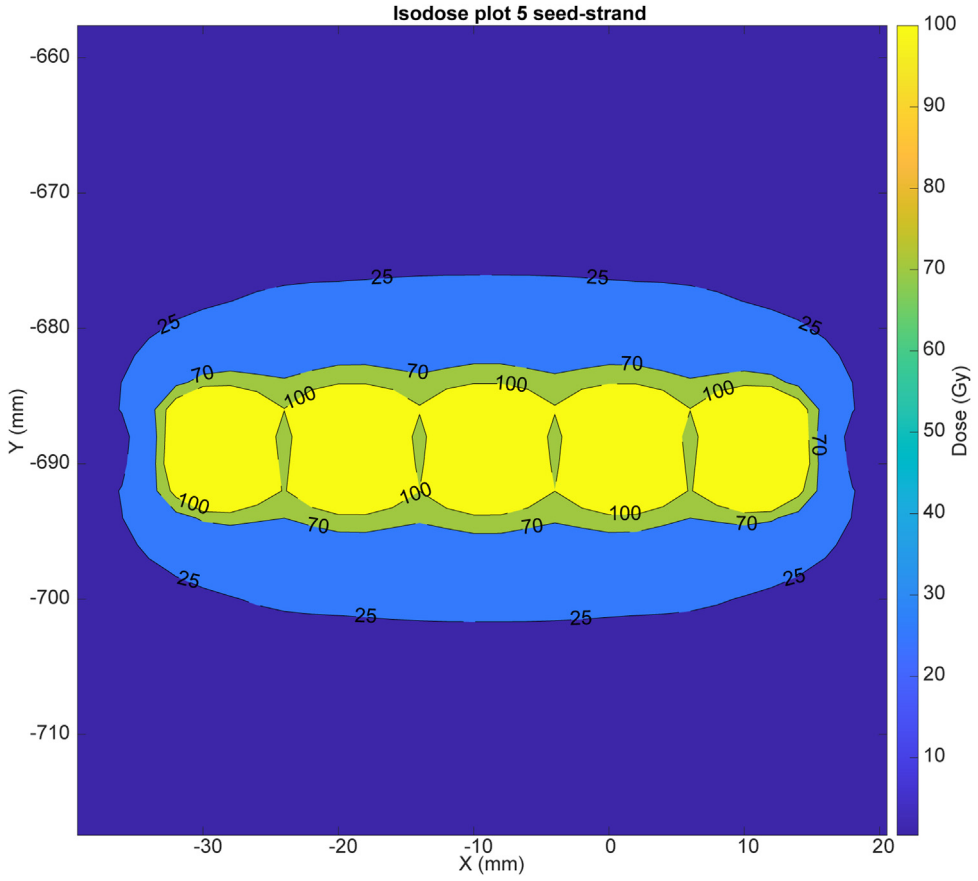

Figure 5. An isodose plot through the centres of a 5 seed strand lined along the X-axis with the isodose lines (100, 70, 25) Gy.

D_{pr} being the prescription dose and N the actual number of needles. The $3 * N$ value changes the dose range dynamically allowing closer needle distances in the late phase of the optimization. Alpha shapes generated with dose grid points fulfilling this condition are used to filter the needle tips with the inShape function.

One loop crawls the needle tips and a nested loop the associated injection points. The objective function is called if the n seeds of a trajectory (calculated by equation 4) are located in the dose range DR too.

The objective function copies the actual target space including the dose distribution of the previously added needles, adds a new needle and calculates the dose. The output is the prescription dose volume inside of the target volume $V_{pr,TV}$ and the relative fraction of it to the whole prescription dose volume V_{pr}. The fraction $\frac{V_{pr,TV}}{V_{pr}} = 1$ signifies, that the total volume of the prescription dose is equal to the volume of the prescription dose inside the target volume. Then no volume of the prescription dose outside of the target volume can be found. A fraction smaller than 1 signifies a volume of prescription dose outside of the target volume.

The needle candidate has to pass the condition

$$\frac{V_{pr,TV}}{V_{pr}} > 0.96 - \frac{3 * N}{100} \tag{8}$$

Then needle configurations with too much unnecessary dose outside of the target volume are avoided. The needle is checked in 1 cm samples along the trajectory for collisions with organ at risks to possibly reject invalid needles unfound by the path planner. These can be trajectories pointing to tip points other than the 6 ones considered by the needle path planner in section 2.2. To save calculation time only the chosen needle candidates are checked. The injection point with the associated tip point maximizing $V_{pr,TV}$ is chosen to be added to the initial plan configuration. The sub-problem is solved and the next one is initialised by refreshing the actual dose. If there is no injection point left satisfying the dose range condition (equation 7), the number of seeds is reduced by 1 to search for a suitable $n - 1$ stranded seed needle. For each sub problem the needle candidate domain is randomly permuted. The optimizer then generates several different plans each time and

a dependence of an ordering effect of the candidate needle domain can be avoided.

2.6 Remove-seeds algorithm

Seeds are located and removed from the treatment plan to reduce the high dose regions ($D > 2 * D_{pr}$) in the target volume. The medians of the dose grid points with a dose $D > 2 * D_{pr}$ and $D < 0.5 * D_{pr}$ are calculated. The needle with the seed closest to the median of these 2 points is found.

For the first and last seed of this needle 8 coordinates c_j are analysed with

$$c_j = \vec{s} \pm 5 * \frac{\vec{n}_i}{|\vec{n}_i|} \pm 2 * \frac{\vec{\lambda}}{|\vec{\lambda}|}, \tag{9}$$

$\vec{n}_i$ being 1 of 2 orthogonal vectors on the needle trajectory, $\vec{\lambda}$ the direction vector of the trajectory and $\vec{s}$ the seed coordinate. They have a distance of 5.4 mm to the seed centre and are counted if the dose at the sample coordinate exceeds the 200% of the prescription dose or if the coordinate is outside of the target volume to define a decision threshold

$$count \geq 8 - n + 2 \tag{10}$$

n being the actual number of seeds of the needle. The threshold is lower for the outlying seeds, because they are likely to be located near of the target volume contour where the dose falls of. The threshold on the other side is higher for the inner seeds that are closer to the high dose region. If both thresholds pass, the higher count decides whether the first or last seed is to be removed. The dose is refreshed and the next 2 outer seeds of the needle are analysed, until no seed exceeds the threshold. It must be noted that removing the first seed is done by removing the last seed and retracting the needle along the trajectory by L_{cc}, the distance from the seeds' centre to centre.

2.7 Needle-depth optimizer

One remaining degree of freedom is the injection depth of the needle. In the actual plan the needle tip points are located on the contour of the target volume or the needles where retracted by removing the first seeds at the resulting needle tip. The aim of this optimizer is to maximize the V100 by covering under-dosed areas by optimizing the source distribution. This should result in a reduced V200 and V150 as the total dose stays constant while the distribution is improved.

The needles with the tip on the contour can be moved forward up to 2 mm with the first seed still remaining inside the target contour. To retract the needle the path length of the last seed to the target contour is sampled in 1 mm steps.

For each 1 mm change of the needles insertion depth the prescription dose volume inside of the target volume $V_{pr,TV}$ is calculated. The needle depth maximizing this value is saved. It is defined that the next needles are alternatingly moved forwards and backwards. The needle with the tip closest to an under-dosed area is analysed first, second with the last seed closest. This is done by analysing the distance matrix of under-dosed voxels inside the target volume to the needle tips or the last seeds for forward or backward movement. The needle with the tip or last seed having the closest distance to one of the under-dosed voxels is chosen to be moved a second time. The algorithm stops if the chosen needle already has been modified by the needle-depth optimizer.

2.8 Coverage optimizer

The coverage of the target volume with the prescription dose is raised by filling under-dosed areas by placement of additional needles with 1 or 2 seeds. For this purpose the needle tips out of the candidate needle domain nearest to the under-dosed voxels must be identified. The function *nearestNeighbour* is used to find the target volume contour points nearest to the under-dosed voxels. The latter are intersected with the needle tips of the candidate needle domain. The seeds must be located *inShape* of the region with a dose smaller than the prescription dose. The candidate needle is checked for collisions with risk structures and has to pass the condition

$$\frac{V_{pr,TV}}{V_{pr}} > 0.7 \tag{11}$$

The $V_{pr,TV}$ is maximized and the algorithm stops if the threshold of $V100' > V100 + \frac{n}{2}$ is surpassed, with n being the number of seeds to be set with the considered needle. The coverage optimizer was only executed in the occasion that the previous plan configuration yielded $V100 < 99\%$.

3 Results

3.1 Path planning and candidate needle domain

The path planning is shown in Figure 6. Figure 6(a) shows the injection points rejected by the sample point sphere inside of the liver contour. Figure 6(c) shows the number of filtered injection points. The total number of injection points is 5699. It is reduced during the path planning to 1568 in 9.7 seconds. In the first risk structure filter described in section 2.2. 44.7% and in the next 290 filter steps 27.8% of all injection points are filtered out. The distance between the injection points is set to a minimum of 2 mm. This reduces the number of injection points to 827 (14.5%) to be considered for the candidate needle domain.

The resulting domain of injection points can be seen in Figure 6(d). The needle candidate domain contains 1971 tip points and the number of possible needle trajectories for 1 seed considered is $1.01 * 10^6$. From 2 to 5 seeds the number of needle trajectories decreases from $8 * 10^5$ to $8 * 10^4$. Figure 7 demonstrates a decreasing number of possible injection points

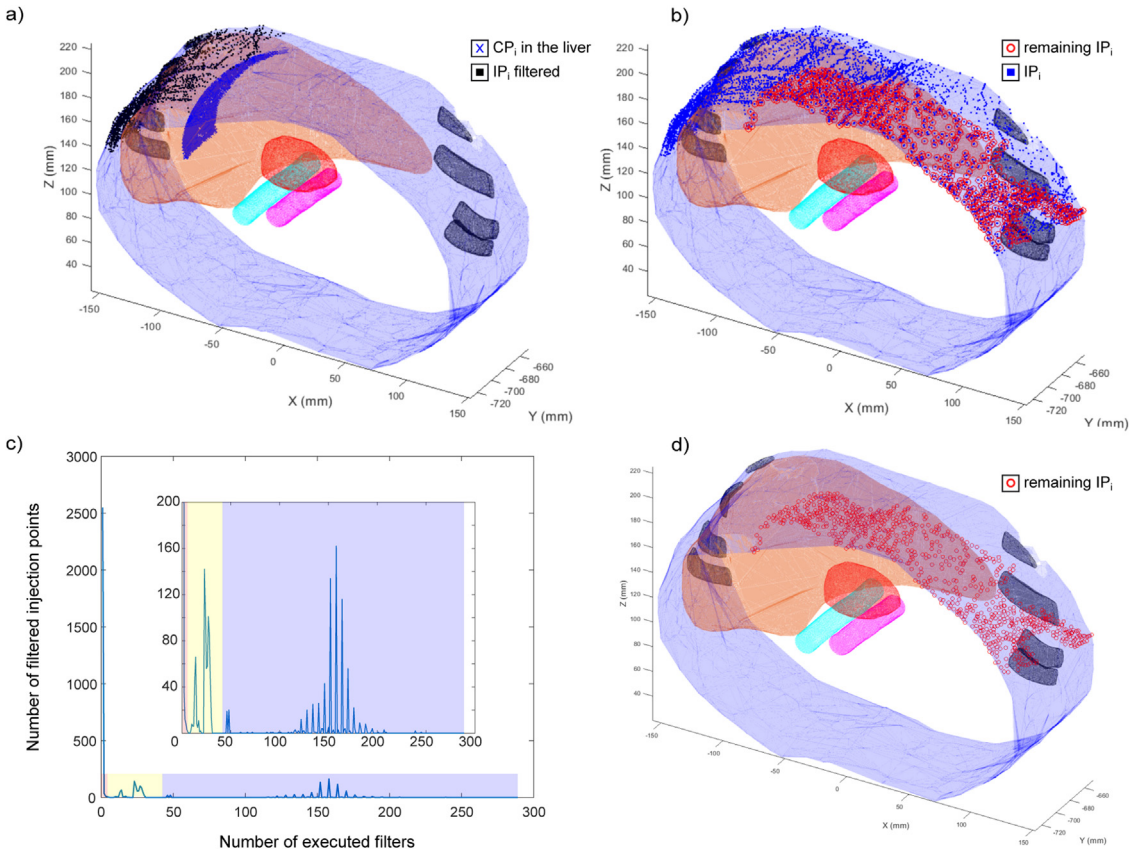

Figure 6. a) The checkpoints (blue x) lie on a sphere and inside the liver. The corresponding injection points IP_i (black dot) are filtered out. b) All considered IP_i (blue dot) and the remaining ones (red circle). c) The number of filtered injection points over the number of executed filters. The inner graph zooms into the range of [0, 200] filtered injection points. d) The remaining IP_i (red circle).

with an increasing number of stranded seeds as the path length inside of the target volume rises. The tip points accessible by the most injection points lie on the target contour opposite to the injection points for 1 seed (Figure 7(a)). For a needle with a 3 seed strand the tip points on the target's right ground can still be reached by needles from upside (Figure 7(b)). For 5 seed strand needles the path length is a more limiting factor and some tip points can still be reached by 40% of the injection points located on the phantoms right side (Figure 7(c)).

The tip points reachable by the most injection points lie on the right part of the target volume near the liver as the majority of injection points is located on the front and left side of the phantom. The path planning and calculation of the candidate needle domain takes 0.7 min.

3.2 Dose modelling

Figure 8 shows the isodose plots of the TPS and Oncentra Prostate (Figure 8(a), (b)), a line plot of the dose along the x-axis (Figure 8(c)) and the resulting gamma analysis (Figure 8(d)). For the purpose of dose comparison the dose was normalized to 290 Gy, the 200% isodose of the standard 145 Gy prescription dose for prostate LDR brachytherapy. The gamma analysis with a threshold of 1% = 2.9 Gy and 1 mm succeeds in 98.5% of the tested pixels.

3.3 Inverse optimization

An example of the volumetric dose parameters V100, V150 and V200 during the optimization along the 4 algorithms marked with different background colours is given in Figure 9. During the greedy optimization every point in the graph marks a new needle added to the solution space. The dose per needle depends on the number of stranded seeds. The first needles contain 5 stranded seeds resulting in a high change of dose parameters. The curve flattens when the number of seeds per needle is reduced. The remove seeds algorithm shows a steep falloff of the V200 about $\approx$ 15% while the V100 decreases about $\approx$ 1%. The depth optimizer increases the V100 and decreases the V150 and V200 slightly. The coverage optimizer increases the V100 over 99% at the costs of the 7% higher V150 and 6% higher V200. Figure 10 displays the overview of a plan configuration with the prescription-isodose volume. The V100, V150, V200 were (99.0, 75.9, 34.2) %

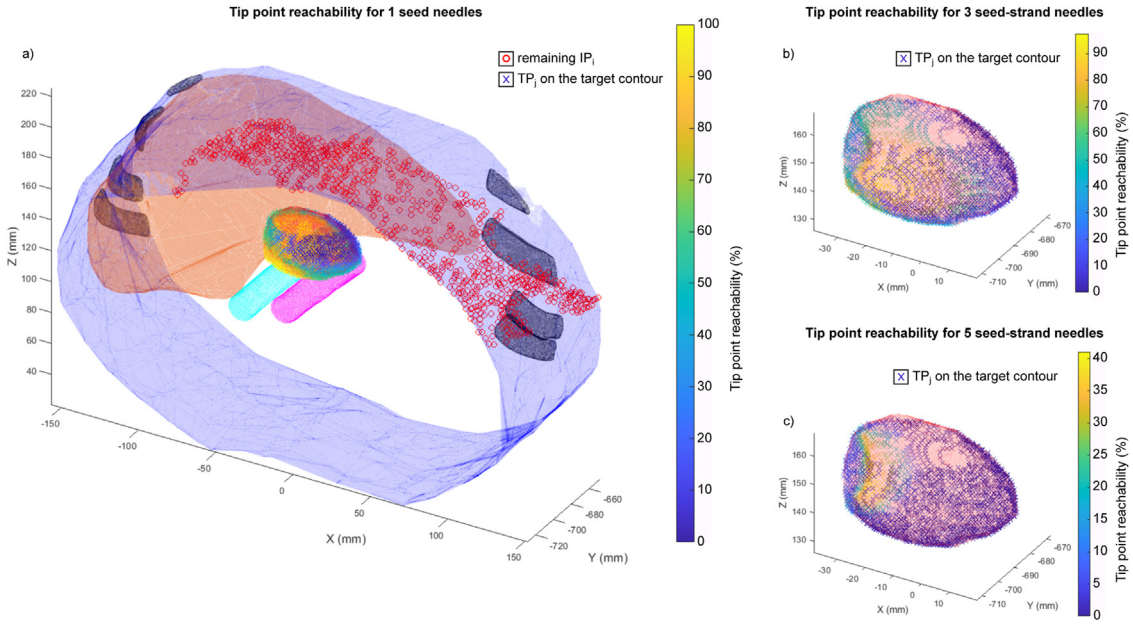

Figure 7. a) The injection points IP_i (red circle) and the tip points (colorbar x) for needles with one seed. The tip point colour indicates the percentage of the injection points able to reach this tip with the needle's seeds located in the target volume. b) and c) The target volume with tip points (colorbar x) for a 3 (b) and 5 (c) seed strand.

and the $D90 = 124.8$ Gy achieved with 13 needles containing 35 seeds.

To test the statistical variability of the system 10 plans with a $(2 * 2 * 2)$ mm^3 grid resolution have been calculated and are displayed in box and whisker plots in Figure 11. The parameters were $V100 = (99.1 \pm 0.3)\,\%$, $V150 = (76.4 \pm 2.5)\,\%$ and $V200 = (44.5 \pm 5.5)\,\%$ (Figure 11(a)). The $D90 = 125.9 \pm 3.6$ Gy was above 120% of D_{pr} yielding a good dose coverage of the target volume (Figure 11(d)). 10.7 ± 1.3 needles with 34.0 ± 0.8 seeds were used (Figure 11(b)). The optimization time median is 2.6 min with a 75% percentile of 3.2 min and 25% percentile of 2.1 min (Figure 11(c)). In 2 cases the optimization time was defined as an outlier with optimization times of 10.5 min and 29.2 min. In these cases the objective function of the coverage optimizer was called repeatedly without fulfilling the required dose conditions e.g. $\frac{V_{pr,TV}}{V_{pr}} > 0.7$. The median of the TPS total running time of 4.4 min includes loading the structure and dose modelling data, calculation of path planning and the candidate needle domain (0.7 min) and the optimization time.

4 Discussion

4.1 Path planning

The order of the path planning filters is designed to efficiently exclude a large number of invalid injection points, as the computation time for each filter depends on the number of tested injection points.

The first risk structures filter using the checkpoints calculated with equation 1 excludes 44.7% of all injection points. As only 1 point per needle trajectory is tested invalid trajectories remain. Check points on an invalid trajectory missed by this check have other parts of the trajectory hitting the risk structure. This is the case for asymmetrically shaped risk structures like the liver. The filters referring to equation 2 consider this issue by adding the standard deviation of the shape points for each room direction in a vector. The latter is pointing towards the room direction with the most outlying shape points. The aorta e.g. with a cylinder shape along the Y-axis has a standard deviation vector pointing strongly in the y-axis and a little bit skew in the x- and z- axis. The raster of $-2 : 0.1 : 2 * \text{std}$ includes about 95% of the points of normally distributed data. For the liver and the ribs this was sufficient to exclude the most injection points automatically. For complex structures it might be necessary to divide them into sub-structures. Each rib was contoured separately instead of contouring the whole thorax as one. Contouring the bones is a task that automatic contouring algorithms could sufficiently achieve nowadays and would be a good application here. The insertion depth of the needles is a parameter to be considered for the treatment planning. In this case of a central metastasis it was sufficient to reject trajectories with the insertion depth for the most posterior contour point in the $-$z direction with 17.5 cm leaving a safety margin of 2.5 cm. Injection points fulfilling this constraint should also reach the lateral tip points with an insertion depth up to 20 cm. For a different geometry this might not be sufficient. As a generalisation every side of the target volume should be considered.

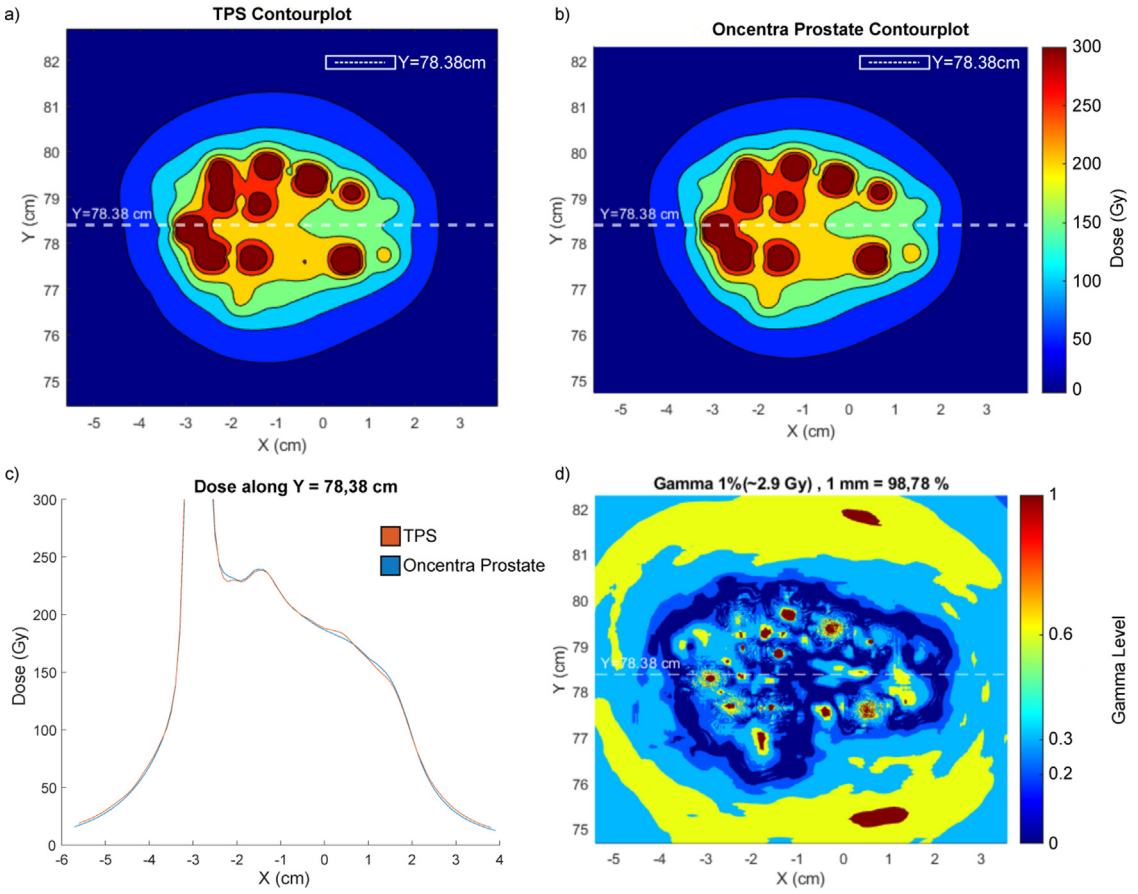

Figure 8. a) and b) The isodose plot of an analysed z-plane with dose calculated by (a): the TPS, b): Oncentra Prostate). The contours show the isodose lines of (300, 250, 200, 150, 100, 50, 0) Gy in the colours red, orange, yellow, green, cyan, blue and dark blue. The white dashed line shows the y-value held constant in the line plot dose over the x-axis in c). d) The gamma plane with the contours of gamma levels (1, 0.6, 0.3, 0.2, 0) in dark red, yellow, cyan, blue and dark blue. The gamma level 1 indicates a failed pixel in the gamma analysis for gamma = 1%, 1 mm with 100% = 290 Gy.

4.2 The candidate needle domain

The candidate needle domain contains about $1.01 * 10^6$ possible needle trajectories resulting out of 827 injection points and 1971 tip points. The state of the art template based approach for prostate low dose rate brachytherapy in contrast works with 125 parallel injection holes on the template. The structure of the candidate needle domain is designed to maintain a fast optimization while dealing with a higher complexity. The candidate needle domain ensures that every needle with the specified number of seeds can be placed inside the target volume.

4.3 Dose modelling

The dose comparison between Oncentra Prostate and the TPS are shown to be comparable with minor differences. One reason for failed pixels is the dose difference in close distance $d < 0.25$ mm to the seeds, where the extrapolated dose values yield a high uncertainty being the case for both treatment systems. In the presented TPS the dose is extrapolated to the seed surface for every angle of the line approximation of the TG-43 formalism showing higher maximum dose values than Oncentra Prostate. 26% of the failed pixels have a dose value over 500 Gy. The extrapolation gives an idea of the amount of dose deposited in the near field of the seed. Clinically the latter is only considered as part of the V200. In the interpolated region of $r = \{2.5, 7\}$ mm the gamma index yields the best values around zero. Here a precise dose calculation is important for the determination and optimization of the monitored dose parameters. Further uncertainty factors are the reconstruction of the treatment plan in Oncentra Prostate resulting in deviations of the seed locations and the dose grid being transformed from the internal coordinate system to Dicom coordinates.

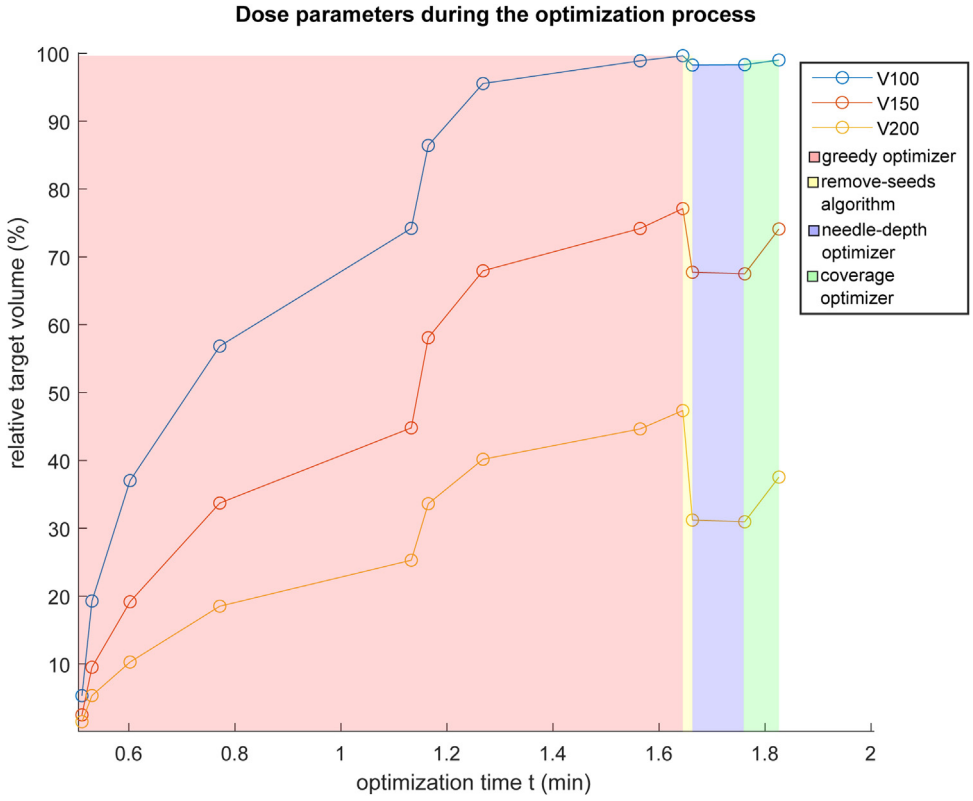

Figure 9. The dose parameters $V100$, $V150$, $V200$ as the percentage of the target volume in blue, red and yellow over the optimization time. The background colours indicate the optimization step executed.

4.4 Inverse optimization

The greedy optimizer was designed to generate an initial treatment plan using the candidate needle domain efficiently. The method of sequentially choosing needles to the solution space bears the risk of getting trapped in a local minimum in the objective function value. This would be the case if a needle is placed in a way that it becomes impossible to cover a specific part of the target volume causing the optimizer to fail. To counteract such behaviour the geometric space to set the next needle is forced to result from the dose distribution of the previous needles as can be seen in equation 7. The relevant dose levels of the latter [25, 70] Gy are displayed in Figure 5. The next needle's tip and seed positions are bound to equation 7. The first needle is an important starting point for the optimization. Therefore the tip point was chosen as the one with the best reachability for needles with 5 stranded seeds and the injection point as the median of the list of possible injection points. This ensures enough possibilities for the next needles to be set in the specified dose region. The lower boundary $0.25 * D_{pr}$ limits the maximum spacing from the needle's tip and their seed positions to the other needles and ensures that the first needles are set near to coplanar which can be seen in Figure 10. This is oriented at the template based approach which appears to be a good strategy to build up dose while avoiding low dose regions in the target centre. The upper boundary of the interval $0.7 * D_{pr} + 3 * N$ ensures that the needles are set with enough space to each other to avoid high dose regions. After a couple of needles the low dose contributions by distanced seeds become more important and the isodoses $0.25 * D_{pr}$ and $0.7 * D_{pr}$ are spreading more towards the target contours. The additional term $3 * N$ of the upper dose limit allows setting the last peripheral needles in a higher dose region. The 10^{th} needle e.g. can be set in the dose region of [25, 100] Gy, the 2^{nd} needle in [25, 76] Gy. The optimizer sets needles with the maximum number of seeds as long as possible before reducing the seed number. This ensures a low number of implantation needles resulting in a faster implantation and lower harm to the patient. With the reduction of the $V200$ the number of seeds can be limited to a reasonable amount.

The statistical results of the 10 treatment plans show a good stability of the optimizer in terms of dose coverage. The $V100 = (99.1 \pm 0.3)\,\%$ and $D90 = 125.9 \pm 3.6\,\text{Gy}$ match our treatment aims with a small uncertainty. Therefore it is unnecessary to calculate multiple treatment plans to optimize the plan. The $V200 = (44.5 \pm 5.5)\,\%$ has a higher variability being influenced by the remove seed algorithm decision in equation 10. If the remove seed algorithm exits without modification of the treatment plan the $V200$ tends to have a higher outcome.

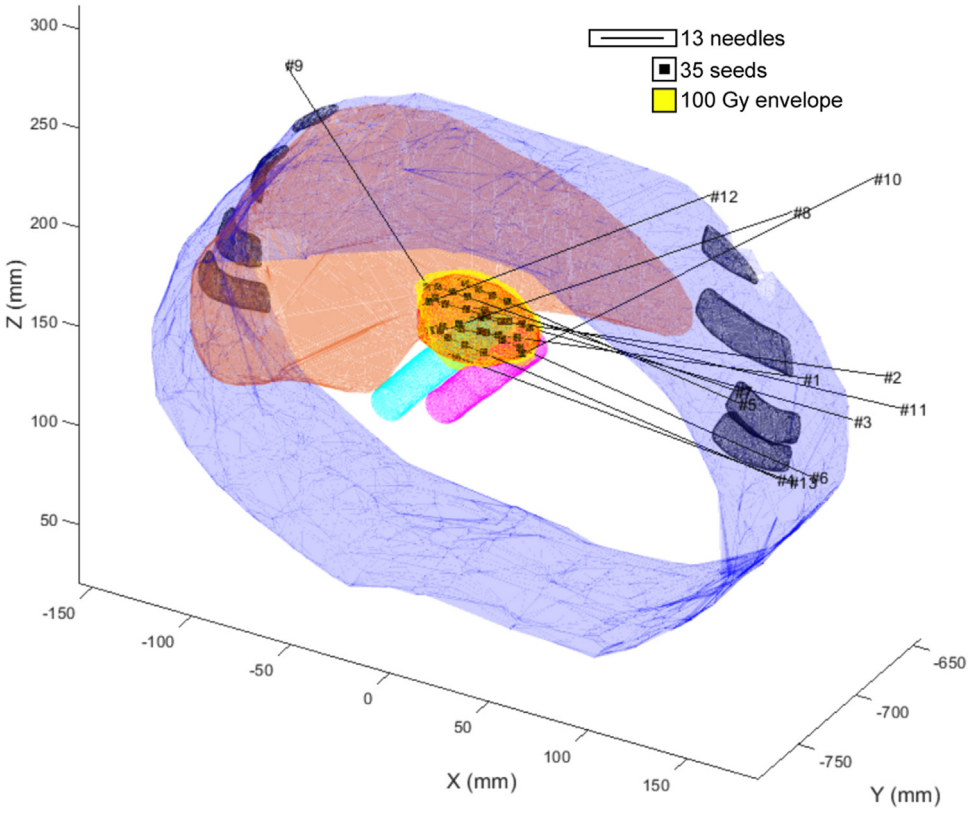

Figure 10. The phantom structures with needles and seeds of one of the 10 treatment plans. The black lines show the 13 needles with 35 seeds (black dot). The 100 Gy dose envelope (yellow) covers the target volume (red).

The remove seed algorithm is designed to reduce the V200 regions caused by the sum of low dose contributions of all seeds in the target centre. The sample coordinates of equation 9 are placed in a range of 5.4 mm. Here the self-contribution of the outlying seed of a 5 seed strand is around 30 Gy. If the dose at this point exceeds the $V200 = 200$ Gy, it can be attributed to the contribution of surrounding seeds. The more of the surrounding sample coordinates fulfil this condition the more dispensable the seed gets. The additional subtraction of n in equation 10 increases the decision threshold for inner seeds. For the outlying seeds a lower threshold is acceptable as these seeds are near the dose falloff at the target volume contour. For 5 stranded seeds the decision threshold increases from 5 to 8 with every seed removed.

The needle depth is varied to optimize the dose distribution with the reduced number of seeds. This can lead to a higher V100 and lower V200. As can be seen in Figure 9 the optimization to this state results in treatment plans with a low V200 and a V100 around 95 to 99 percent. Due to the depth optimizer the V100 increases and the V150 and V200 decrease slightly. The coverage optimizer increases the V100 at the cost of a higher V200.

All algorithms are implemented as functions. In a real optimization procedure one would combine these functions to get the most appropriate treatment plan.

A comparable TPS to the presented one is using a simulated annealing optimizer in [14]. Here the catheters are placed virtually by the physician before the optimization process. Then the seed positions on these needles are considered by the simulated annealing optimizer with a fixed number of seeds. The optimization is done varying the number of seeds and comparing the DVH. The organ at risks can be spared by the simulated annealing as well. This TPS in contrast considers the catheter placement, the total number of needles and seeds as part of the optimization process.

4.5 Limitations of the TPS

The optimizer's performance depends on the prescription dose. If the latter is changed the optimizers have to be adapted. In the greedy optimizer this can be seen in equation 7. The distance of the dose envelopes $0.25 * D_{pr}$ to $0.7 * D_{pr}$ increases with a high prescription dose and decreases with a lower one because the seeds' dose falloff is exponentially decreasing.

The system is in principle independent of the tumour site and could be used for tumours in the thorax, head and neck or abdomen after considering the optimization parameters. However the TPS performance is unknown to the latter and practically optimisation templates for each site with different surrounding obstacles might be useful. With the raising

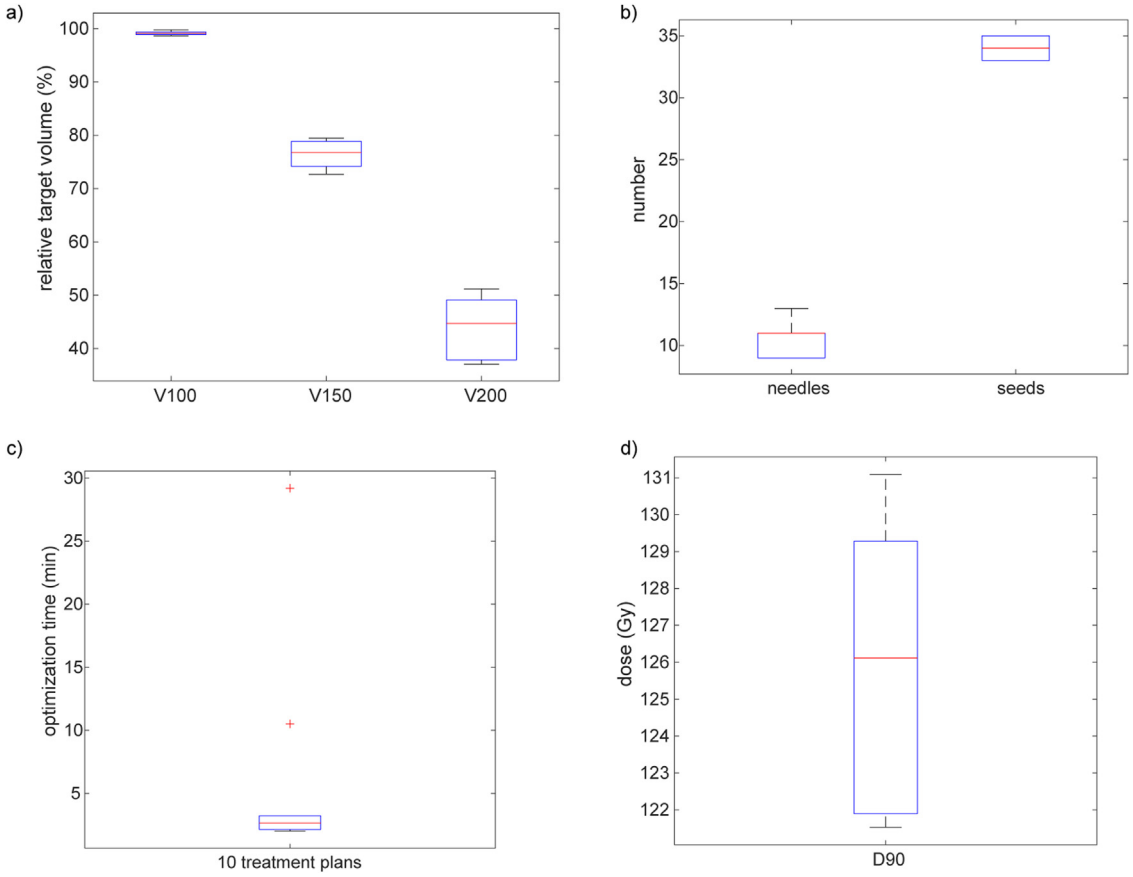

Figure 11. Box and whisker plots for the statistic of 10 treatment plans. The red line indicates the median, the bottom and top edges of the boxes the 25th and 75th percentiles. The whiskers extend to the extreme data values not considered (outliers). a) The dose parameters $V100$, $V150$ and $V200$ as the percentage of the target volume. b) The number of needles and seeds used. c) The optimization time for the 10 treatment plans with two outliers (red crosses). d) The statistic of the $D90$ dose parameter.

number of risk structures the domain of the optimizer shrinks and the treatment planning gets more difficult. Then the path planning algorithm could be adapted in a way that only needle trajectories able to reach parts of the target volume are accepted. In a real patient this might be necessary for the liver metastasis as well. Then more organs at risk like the pancreas and stomach are considered and lateral trajectories are rejected by the path planner. Another important parameter is the allowed insertion depth. In this case no trajectories have been rejected due of the insertion depth and the most needles were set from the side as the most needles with 5 seed strands are possible from there. This strategy sets the focus on minimizing the total number of needles used by allowing as much needles as possible. Then the optimizer is able to choose needles with long seed strands adapted to a target volume asymmetrically shaped e.g. elliptically. Another possible strategy would be to constrain the insertion depth or to introduce a weighting factor on each needle to prefer needles with short insertion depths. The total number of used needles might increase while the needle placement accuracy increases due to a decreased placement uncertainty. In contrast to the central metastasis in this work the latter strategy makes sense if the tumour is spherical shaped and laterally located near the skin. Then the distance from the preferred implantation side to the metastasis could be measured in the CT images and used as an insertion depth constraint.

However clinical studies must show a benefit for the patient undergoing the seed implantation. In our research we aim to use LDR brachytherapy for patients in the oligometastatic state with a maximum of 3-5 metastases [28]. Phase II studies indicate a survival benefit for patients with local treatment for unresectable colorectal liver metastases treated with tumour ablation [29] and for stereotactic ablative radiotherapy for all metastatic sites [30].

The dose formalism TG-43 approximates the tissue as water equivalent, which results in a larger dose error in tissues with higher and lower density as the bones or the air filled lung. The inter-seed interaction as the presence of the seeds as non-water equivalent objects near to each other is neglected as well.

5 Conclusion

We here present an inverse treatment planning system capable to generate clinically acceptable plans in a reasonable amount of time while being independent of an injection template or defined injection area. A path planner locates the trajectories able to reach the target volume while sparing risk structures from puncture. An inverse optimizer searches for an acceptable combination of needle trajectories and seeds to cover the target volume with the prescription dose and limit the high dose regions inside. The TPS takes advantage of the high degrees of freedom provided by robotic navigation tools. This gives a high flexibility to treat tumours difficult to reach by robotic minimally invasive low-dose-rate brachytherapy.

Acknowledgments

This research project is part of the Research Campus M^{2}OLIE and funded by the German Federal Ministry of Education and Research (BMBF) within the Framework "Forschungscampus: public-private partnership for Innovations" under the funding code 13GW0092D.

The funding source took no role in the data analysis or study design.

References

[1] Mottet N, Bellmunt J, Bolla M, Briers E, Cumberbatch MG, Santis MD, et al. EAU-ESTRO-SIOG guidelines on prostate cancer. Part 1: Screening, diagnosis, and local treatment with curative intent. Eur Urol 2017;71:618–29, http://dx.doi.org/10.1016/j.eururo.2016.08.003.

[2] Grimm P, Billiet I, Bostwick DA, Dicker P, Frank S, Immerzeel J, et al. Comparative analysis of prostate-specific antigen free survival outcomes for patients with low, intermediate and high risk prostate cancer treatment by radical therapy. Results from the Prostate Cancer Results Study Group. BJU Int 2012;109:22–9, http://dx.doi.org/10.1111/j.1464-410X.2011.10827.x.

[3] Buergy D, Schneiberg V, Schaefer J, Welzel G, Trojan L, Bolenz C, et al. Quality of life after low-dose rate-brachytherapy for prostate carcinoma – long-term results and literature review on QLQ-C30 and QLQ-PR25 results in published brachytherapy series. Health Qual Life Outcomes 2018;16:21, http://dx.doi.org/10.1186/s12955-018-0844-8.

[4] Stish BJ, Davis BJ, Mynderse LA, McLaren RH, Deufel CL, Choo R. Low dose rate prostate brachytherapy. Transl Androl Urol 2018;7 http://tau.amegroups.com/article/view/18019.

[5] Martinez-Monge R, Nag S, Nieroda CA, Martin EW. Iodine-125 brachytherapy in the treatment of colorectal adenocarcinoma metastatic to the liver. Cancer 1999;85:1218–25, http://dx.doi.org/10.1002/(SICI)1097-0142(19990315)85:6<1218::AID-CNCR2>3.0.CO;2-F.

[6] Nori ZT, Hilaris D, Manolatos B, Linares S, Harrison L, Anderson L, et al. Treatment of primary unresectable carcinoma of the pancreas with I-125 implantation. Int J Rad Oncol Biol Phys 1989;17:931–5, http://dx.doi.org/10.1016/0360-3016(89)90138-7.

[7] Shipley WU, Nardi GL, Cohen AM, Ling CC. Iodine-125 implant and external beam irradiation in patients with localized pancreatic carcinoma. A comparative study to surgical resection. Cancer 1980;45:709–14, http://dx.doi.org/10.1002/1097-0142(19800215)45:4<709::AID-CNCR2820450416>3.0.CO;2-5.

[8] Theodore SB, Dickman N, Sonntag CA, Thomas VK, Lam T, Rogers SCL. Surgery and permanent 125I seed paraspinal brachytherapy for malignant tumors with spinal cord compression. Int J Rad Oncol Biol Phys 2002;54:505–13, http://dx.doi.org/10.1016/s0360-3016(02)02961-9.

[9] Hilaris BS, Nori D, Martini N. Intraoperative radiotherapy in stage I and II lung cancer. Sem Surg Oncol 1987;3:22–32, http://dx.doi.org/10.1002/ssu.2980030104.

[10] Zhongmin W, Yu L, Fenju L, Kemin C, Gang H. Clinical efficacy of CT-guided iodine-125 seed implantation therapy in patients with advanced pancreatic cancer. Eur Radiol 2010;20:1786–91, http://dx.doi.org/10.1007/s00330-009-1703-0.

[11] Cao Q, Wang H, Meng N, Jiang Y, Jiang P, Gao Y, et al. CT-guidance interstitial 125Iodine seed brachytherapy as a salvage therapy for recurrent spinal primary tumors. Rad Oncol 2014;9:301, http://dx.doi.org/10.1186/s13014-014-0301-8.

[12] Junjie W, Shude C, Ruoyu W, Guangjun Z, Kaixian Z, Bin H, et al. Expert consensus on computed tomography-assisted three-dimensional-printed coplanar template guidance for interstitial permanent radioactive 125I seed implantation therapy. J Cancer Res Therapeut 2019;15:1430–4.

[13] Ma X, Yang Z, Jiang S, Huo B, Cao Q, Chai S, et al. Effectiveness and safety of a robot-assisted 3D personalized template in 125I seed brachytherapy of thoracoabdominal tumors. J Contemp Brachytherapy 2018;10:368–79, http://dx.doi.org/10.5114/jcb.2018.77957.

[14] Ma X, Yang Z, Jiang S, Zhang G, Huo B, Chai S. Hybrid optimization based on non-coplanar needles for brachytherapy dose planning. J Contemp Brachytherapy 2019;11:267–79, http://dx.doi.org/10.5114/jcb.2019.86167.

[15] Smakic A, Rathmann N, Kostrzewa M, Schönberg SO, Weiß C, Diehl SJ. Performance of a robotic assistance device in computed tomography-guided percutaneous diagnostic and therapeutic procedures. Card Vasc Interv Radiol 2018;41:639–44, http://dx.doi.org/10.1007/s00270-017-1841-8.

[16] Rothfuss A, Oesterle O, Bürgy D, Nwankwo C, Schneider F, van Poelgeest A, et al. System and path planning algorithm for low-kV X-ray free-form surface irradiation. Int J Med Robotics Comput Assist Surg 2018;14:e1899, http://dx.doi.org/10.1002/rcs.1899.

[17] Podder TK, Beaulieu L, Caldwell B, Cormack RA, Crass JB, Dicker AP, et al. AAPM and GEC-ESTRO guidelines for image-guided robotic brachytherapy: report of Task Group 192. Med Phys 2014;41:101501, http://dx.doi.org/10.1118/1.4895013.

[18] Siauw T, Cunha A, Berenson D, Atamtürk A, Hsu I-C, Goldberg K, et al. NPIP: a skew line needle configuration optimization system for HDR brachytherapy. Med Phys 2012;39:4339–46, http://dx.doi.org/10.1118/1.4728226.

[19] Olesen JT. DICOM-RT to Matlab. https://github.com/ulrikls/dicomrt2matlab [last accessed 29.03.21], n.d.

[20] Edelsbrunner H, Mücke EP. Three-dimensional alpha shapes. ACM Trans Graph 1994;13:43–72, http://dx.doi.org/10.1145/174462.156635.

[21] alphaShape. Polygons and polyhedra from points in 2-D and 3-D. https://ch.mathworks.com/help/matlab/ref/alphashape.html [last accessed 26.03.21], n.d.

[22] Stone NN, Potters L, Davis BJ, Ciezki JP, Zelefsky MJ, Roach M, et al. Customized dose prescription for permanent prostate brachytherapy: insights from a multicenter analysis of dosimetry outcomes. Int J Rad Oncol Biol Phys 2007;69:1472–7, http://dx.doi.org/10.1016/j.ijrobp.2007.05.002.

[23] inShape. Determine if point is inside alpha shape. https://ch.mathworks.com/help/matlab/ref/alphashape.inshape.html [last accessed 30.03.21], n.d.

[24] Fuller DB, Koziol JA, Feng AC. Prostate brachytherapy seed migration and dosimetry: analysis of stranded sources and other potential predictive factors. Brachytherapy 2004;3:10–9, http://dx.doi.org/10.1016/j.brachy.2004.02.003.

[25] Rivard MJ, Coursey BM, DeWerd LA, Hanson WF, Saiful Huq M, Ibbott GS, et al. Update of AAPM Task Group No. 43 Report: a revised AAPM protocol for brachytherapy dose calculations. Med Phys 2004;31:633–74, http://dx.doi.org/10.1118/1.1646040.

[26] Rivard MJ, Ballester F, Butler WM, DeWerd LA, Ibbott GS, Meigooni AS, et al. Erratum: "Supplement 2 for the 2004 update of the AAPM Task Group No 43 Report: Joint recommendations by the AAPM and GEC-ESTRO" [Med. Phys. Vol 44 (9) e297–e338 (2017)]. Med Phys 2018;45:971–4, http://dx.doi.org/10.1002/mp.12728.

[27] Yoo S, Kowalok ME, Thomadsen BR, Henderson DL. Treatment planning for prostate brachytherapy using region of interest adjoint functions and a greedy heuristic. Phys Med Biol 2003;48:4077–90, http://dx.doi.org/10.1088/0031-9155/48/24/006.

[28] Guckenberger M, Lievens Y, Bouma AB, Collette L, Dekker A, deSouza NM, et al. Characterisation and classification of oligometastatic disease: a European Society for Radiotherapy and Oncology and European Organisation for Research and Treatment of Cancer consensus recommendation. Lancet Oncol 2020;21:e18–28, http://dx.doi.org/10.1016/S1470-2045(19)30718-1.

[29] Ruers T, Van Coevorden F, Punt CJA, Pierie J-PEN, Borel-Rinkes I, Ledermann JA, et al., E.O. for Research, Treatment of Arbeitsgruppe Lebermetastasen und tumoren in der Chirurgischen Arbeitsgemeinschaft Onkologie (ALM-CAO) Cancer (EORTC) Gastro-Intestinal Tract Cancer Group, the National Cancer Research Institute Colorectal Clinical Study Group (NCRI CCSG), Local Treatment of Unresectable Colorectal Liver Metastases: Results of a Randomized Phase II Trial. J Natl Cancer Inst 2017;109, http://dx.doi.org/10.1093/jnci/djx015.

[30] Palma DA, Olson R, Harrow S, Gaede S, Louie AV, Haasbeek C, et al. Stereotactic ablative radiotherapy for the comprehensive treatment of oligometastatic cancers: long-term results of the SABR-COMET Phase II Randomized Trial. J Clin Oncol 2020;38:2830–8, http://dx.doi.org/10.1200/JCO.20.00818.

Available online at www.sciencedirect.com

ScienceDirect